Submitted to *Materials*. Pages 1 - 21.

OPEN ACCESS

Article

Preparation and Characterization of Li-ion Graphite Anodes using Synchrotron Tomography

Tim Mitsch [1,*], Yvonne Krämer [1], Julian Feinauer [1,2], Gerd Gaiselmann [2], Henning Markötter [3], Ingo Manke [3], Andreas Hintennach [4] and Volker Schmidt [2]

[1] Deutsche ACCUmotive GmbH & Co. KG, Neue Straße 95, 73230 Kirchheim unter Teck, Germany
[2] Institute of Stochastics, Ulm University, Helmholtzstr. 18, 89069 Ulm, Germany
[3] Helmholtz-Zentrum Berlin, Hahn-Meitner-Platz 1, 14109 Berlin, Germany
[4] Daimler AG, HPC H152, Mercedesstr. 137, 70367 Stuttgart, Germany

* Author to whom correspondence should be addressed; tim.mitsch@daimler.com, phone: +49 176 30905697, fax: +49 711 3052123291

Version May 26, 2014 submitted to Materials. *Typeset by LaTeX using class file mdpi.cls*

Abstract: We present an approach for multi-layer preparation to perform microstructure analysis of Li-ion cell anode active material using synchrotron tomography. All necessary steps from disassembly of differently housed cells (pouch and cylindrical), via selection of interesting layer regions to separation of graphite-compound and current collector are described in detail. The proposed stacking method improves the efficiency of synchrotron tomography by measuring up to ten layers in parallel, without loss of image resolution nor quality, resulting in a maximization of acquired data. Additionally we perform an analysis of the obtained 3D volumes by calculating microstructural characteristics like porosity, tortuosity and specific surface area. Due to a large amount of measurable layers within one stacked sample, differences between aged and pristine material (e.g. significant differences in tortuosity and specific surface area while porosity remains constant) as well as homogeneity of the material within one cell could be recognized.

Keywords: graphite; synchrotron tomography; Li-ion; preparation; degradation; porosity; tortuosity; multi-layer

---

1. Introduction

In recent times electrochemical energy storage is becoming more important, especially for usage in e-mobility applications such as pure electrical, plug-in-hybrid or mild-hybrid vehicles. The requirements regarding long-life (usage time $\geq 10\,\text{years}$) and high energy density are dominantly fulfilled by Li-ion cells. Furthermore due to their complicated ageing behavior [1,2] they are in focus of many researchers to gain better understanding of the ageing process.

During lifetime of Li-ion cells a lot of ageing mechanisms [1,2] occur which affect different components like anode or cathode active material, separator, current-collector or electrolyte. These mechanisms interact in a very complex way. Notably graphite, which is mainly used as anode material, is involved in many ageing processes [1]. Literature dominantly shows well-known but only partly understood mechanisms like growth of SEI (solid electrolyte interface) at the boundary between graphite particles and electrolyte [3–5], lithium deposition caused by high current or low temperature charging [6–8], micro-cracking of graphite-particles caused by massive electrical usage [9] and structural changes of anode active material due to multiple reasons.

To get a closer insight into microstructure of anode active material we use synchrotron tomography [10–19]. Besides the qualitative impressions that one can get from visual inspection of tomographic 3D images we calculate structural characteristics of the samples to obtain a quantitative statement of the state of the material samples. In particular, we look at the spherical contact distribution function for the graphite material, which is closely related to the diffusive behavior of the graphite phase. Furthermore, we calculate the tortuosity that is an important characteristic related to the transport of ions in porous media [20]. A change in the tortuosity for degraded material can be explained by cracks and fractures in the structure.

The paper is organized as follows. In Section 2 we give an overview of the necessary steps for the disassembling of different types of Li-ion cells. Furthermore, a promising approach of surface modification for graphite to qualify the presence of lithium deposition is introduced in Section 2.4. Accordingly we discuss the preparation of samples to stacks to improve the efficiency of synchrotron tomography in Section 3. Up to ten samples can be stacked together, in order to be measured in parallel. The experimental setup, i.e., the samples that are extracted from pristine and aged cells as well as the necessary post-processing methods, like reconstruction and binarization are presented in Section 4. Finally, in Section 5 we discuss the results of several structural analyses like the calculation of tortuosity and spherical contact distribution functions. These analysis methods allow a quantitative description of the samples and show the potential of synchrotron tomography in combination with refined preparation techniques as a valuable tool for the investigation and characterization of functional materials.

2. Extraction of Samples

In this section we describe the procedure to obtain anode samples from different types of Li-ion cells for structural analysis. For purposes of comparability all analyzed cells were discharged to 0 % SOC (state-of-charge) using CC-CV (constant current constant voltage) discharge procedure with the cut-off voltage given in the datasheet delivered by the manufacturer. The method for extraction of samples from anode material will be described in detail.

2.1. Cell Disassembly

To minimize degradation caused by the presence of oxygen and humidity we disassembled all cells in a glovebox (mBraun MB-200B, $H_2O < 4\,\mathrm{ppm}$,$O_2 < 4\,\mathrm{ppm}$).

Automotive Li-ion pouch cells were opened with a ceramic scalpel to avoid unwanted shorts and further structural changes. After removal of the upper pouch foil the electrodes can be separated and analyzed optically.

The aluminium housing of cylindrical cells was sliced next to the positive terminal using a self-constructed tool. Then the positive terminal and its connection to cathode active material were separately disassembled. Finally the aluminium case has to be rolled down using a small pliers. To ensure non-destructive disassembly we controlled the temperature of the cell as the best indicator for shorts. The used setup consists of a PT100 thermal-resistor connected to a PicoTechology® PT-104 data logger visualized by a common notebook. If temperature exceeded $35\,^{\circ}\mathrm{C}$ we did not use the cell for further analysis.

2.2. Sample Selection

As shown in Figure 1(a) from one pouch cell we extracted multiple samples with a size of $10\,\mathrm{mm}$ x $10\,\mathrm{mm}$ using a ceramic scalpel. In case of cylindrical cells several equally-sized ($10\,\mathrm{mm}$ x $10\,\mathrm{mm}$) samples were sliced from equidistant intervals d of the jellyroll, see Figure 1(b).

Subsequently all samples were washed with dimethyl carbonate (DMC).

Figure 1. Anode sample selection from different type of cells

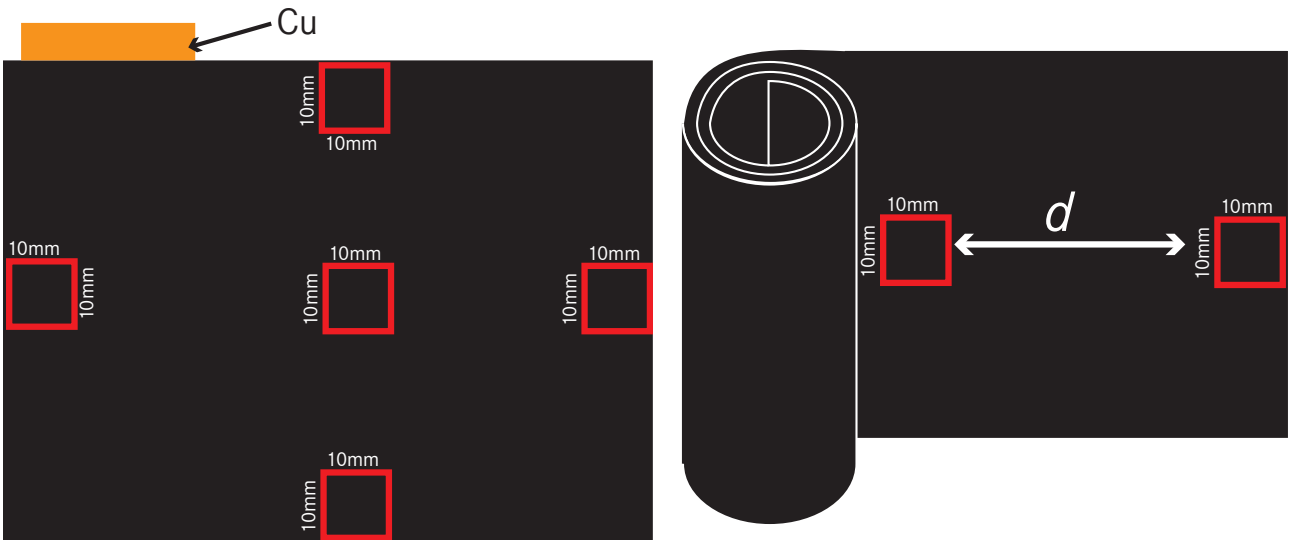

(a) Pouch cell (b) Cylindrical cell

2.3. Separation of Graphite Layers

The structure of an anode layer used in Li-ion cells usually consists of a copper foil coated with a mixture of graphite and binder on both sides, see Figure 2(a). Metals like copper have a high density and therefore X-ray beams used in synchrotron tomography are not able to pass through. To sustain better image quality from anode sample it is mandatory to separate copper foil and graphite layers. Three different methods were compared. An overview is shown in Table 1.

Table 1. Methods for separation of graphite from copper foil

tested methods	**sample size**	**shape**
scrape off Cu	undefined	crimped
freeze with N_2 and scrape off Cu-metal	undefined	crimped
chemical treatment with (HNO_3; 65%)	defined	flat

To achieve reproducible results, defined sample sizes and flat shapes are essential. Therefore chemical treatment using nitric acid (HNO_3; 65%) yielded the best graphite monolayer [10,21]. Depending on the thickness of monolayers, type of degradation (e.g. lithium deposition) and binder used by manufacturer we received the best samples using $5\,\mathrm{ml}$ of demineralized water and three to ten drops of HNO_3 resulting in a dilute nitric acid ($2-6\,\%$) solution. After $5\,-30\,\mathrm{s}$ the copper foil dissolved. Both graphite layers were washed twice with demineralized water and once using propane-2-ol (C_3H_7OH), while constantly paying attention to the orientation of the layers (see pink markers in Figure 2(b)). Finally the separated layers were stored on a small sheet of paper for at least $10\,\mathrm{min}$ in order to dry.

Figure 2. Separation of two graphite layers out of one sliced sample

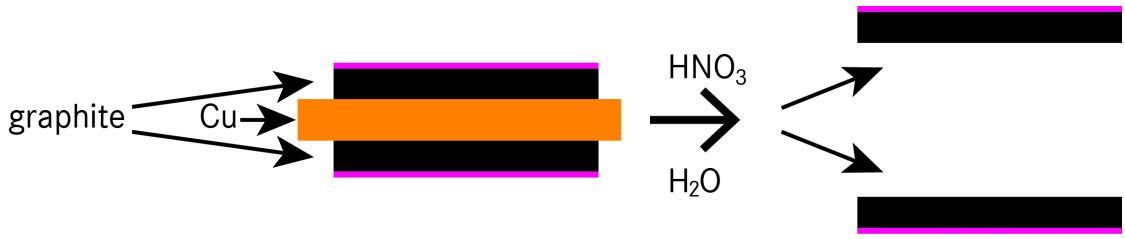

(a) Structure of anode layer

(b) Separated active material after application of HNO_3; 65%

2.4. Surface Modification

Metallic lithium which was formed as a result of electrochemical plating during cycling of an electrode is not visible in neutron-diffraction experiments. But there are some paths to enhance the visibility by adding complexes and/or different metal-ions on the metallic lithium parts. With a surface modification using e.g. glucosoamines the metallic lithium deposition can be made visible in neutron experiments.

Deposition of metallic lithium is primarily a diffusion triggered process. To verify the proposed surface modification procedure using glucosamines the cells were cycled 20 times ($1\,\mathrm{C}$ charge- and $1\,\mathrm{C}$ discharge current at potential range $3\,\mathrm{V}-4.2\,\mathrm{V}$) at ambient temperature of $-10\,^{\circ}\mathrm{C}$ to ensure the presence of metallic lithium on anode surface.

Figure 3. (a) *N*-(Methylnitrosocarbamoyl)-α-D-glucosamine - (b) FT-IR spectra of a pristine electrode and the surface modified parts which exhibited metallic lithium plating

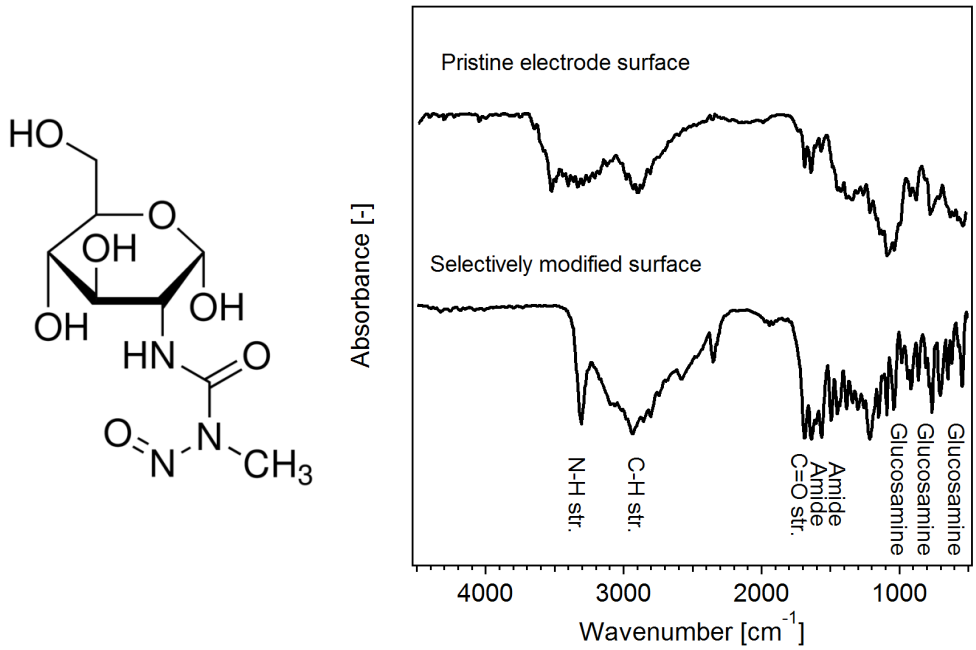

(a) (b)

The additives were used with a slight excess to ensure a homogeneous coating of the lithium-plated parts of the electrode. A homogeneous coating proved to be essential for the detailed investigation of the surface.

N-(Methylnitrosocarbamoyl)-α-D-glucosamine (STZ; Sigma-Aldrich, see Figure 3(a)) was used for the selective modification of the surfaces ex-situ. A solution of STZ in DMC (1M) was prepared in an argon-filled glovebox. About 2 wt.-% of a solution of predispersed surfactants (Triton X-109, Triton X-209; 1:1 by volume) in EC:DMC (1:1 by volume, 10 wt.-%) were added with stirring. This solution could be directly added into the electrolyte between the electrodes. For a homogeneous mixing of the additive with the electrolyte and to ensure a homogeneous wetting of the electrodes it is important to allow a standing time of about $30\,\mathrm{min}$ after the injection of STZ-solution was completed. An adjacent heating step ($38\,^{\circ}\mathrm{C}$, $15\,\mathrm{min}$) initiated the surface modification. This process is schematically shown in Figure 4. Note that no electrochemical cycling was performed after the additive was added. This is the reason for the low electrochemical stability of the glucosamine, while the stability at open circuit potential is high enough for a safe preparation of the samples.

Figure 4. Schematic surface modification process

FT-IR microscopy was applied for the investigation of the influence of the surface modification at lateral resolution, where a HJY LabRAM HR with FT-IR module was used.

While the upper spectrum of Figure 3(b) displays typical bands of the as-prepared electrode including parts with metallic lithium, the lower spectrum in Figure 3(b) exhibits carbonyl peaks ($\mathrm{C} = \mathrm{O}$) at $1628\,\mathrm{cm}^{-1}$ and hydroxyl peaks ($\mathrm{C} - \mathrm{H}$) at about $3304\,\mathrm{cm}^{-1}$. Significant differences could be observed between parts of the electrode where lithium-plating and pristine parts occurred. With an adjacent mapping technique larger areas of electrodes (about $1.5\,\mathrm{cm} \times 1.2\,\mathrm{cm}$) were investigated to validate the surface modifying effect of STZ. The LC-MS analysis of the electrolyte showed that the consumption of consumed STZ could be correlated very well with the amount of metallic lithium which was deposited onto the surface of the electrodes.

3. Multilayer Preparation

Synchrotron tomography is a useful tool to obtain microstructural characteristics of Li-ion anode material. To maximize the efficiency we prepared the anode samples in a multilayer stack. This gives us the opportunity to compare different kinds of aged cells, various anode materials from different manufactures and verify the homogenenity of the production processes.

Therefore our approach is to stack the anode layers to measure several samples in parallel. This means that we obtain one image for all samples inside one stack. Hence the anode samples inside one stack have to be devided sharply with a separator layer in between. The additional layers have to feature a non-particle based microstructure for good visibility and contrast against graphite. In this work we investigate the influence of different separation materials and stacking properties.

3.1. Separation Materials

Focusing on the microstructure the following materials were selected:

1. adhesive tape (lattice structure of backing film)
2. Li-ion separator materials (microporous polymer mebrane [22])
3. cellulose papers (fabric structure)

Beside the discussed microstructural properties above we identified the following characteristics which are important for a promising stacking preparation: 1) thickness, 2) stability of the stack, 3) stickiness and 4) sliceability.

The properties of the investigated materials are summarized in Table 2.

Table 2. Overview of separation materials and stack properties

material	**separator thickness**	**max. layers***	**stability of stack**	**stickiness**		**sliceability**
				add. glue	**property**	
single side adhesive tape	45 µm	9	-	no	no	++
double side adhesive tape	35 µm	10	++	no	no	- -
Celgard(r) 2325	25 µm	11	- -	yes	primer	0
Celgard(r) 2400	25 µm	11	- -	yes	primer	0
Celgard(r) 2500	25 µm	11	- -	yes	primer	0
Greaseproof paper	60 µm	7	++	yes	good	+
Wrapping tissue	35 µm	10	+	yes	good	+
reprographic paper	100 µm	5	++	yes	good	+

*: assuming an anode-thickness of 60 µm

3.2. Layer Stacking

To realize a good resolution the optimal sample dimensions for synchrotron tomography should be a cylinder (∅ $1\,\mathrm{mm}$, h: $1\,\mathrm{mm}$). Thus, the thickness of the complete stack can be calculated using the following formula:

$$d_{\mathrm{Stack}} = n \cdot d_{\mathrm{anode-layer}} + (n+1) \cdot d_{\mathrm{separation}}$$

with n number of anode samples per stack, $d_{\mathrm{anode-layer}}$ thickness of anode layer and $d_{\mathrm{separation}}$ thickness of separation material.

Generally stacking was performed by alternating separation layers ($25\,\mathrm{mm}$ x $25\,\mathrm{mm}$) and anode samples ($10\,\mathrm{mm}$ x $10\,\mathrm{mm}$). At the bottom and the top of the stack a separation layer is essential to ensure stability. A maximum overlap occurs between all anode samples inside one stack. Furthermore it is important to ensure the correct orientation (see Figure 2(b), pink marker) of each layer.

Note that for stack preparation using Li-ion separator materials and cellulose papers additional rapid glue (LocTite® 4850) based on cyanacrylates was used. Each stack was marked on the top and stored for $24\,\mathrm{h}$.

We assume that there is no effect on electrode morphology using cyanacrylates based glue. This was confirmed by comparison of adhesive tape and glue based preparation methods - no significant differences could be noticed.

3.3. Stack Slicing and Final Setup

As described above the final geometry of the anode stack should be cylindric. To achieve an approximation of $1\,\mathrm{mm}$ in diameter we applied a rectangular shape. By using Pythagorean theorem the length of the edge was calculated to $0.7\,\mathrm{mm}$. The sequence of the slices is shown in Figure 5(a).

Afterwards we were able to monitor the size of the stack by using an optical microscope (Leica) or SEM imaging, see Figure 6. Finally the prepared anode stack was fixed on a specific sample holder with a little amount of hot or rapid glue to perform synchrotron measurement. Figure 5(b) shows the final probe, which was applied to the tomography setup.

Figure 5. (a) Necessary cuts of stacked probe to realize final geometrics, (b) Final preparation setup

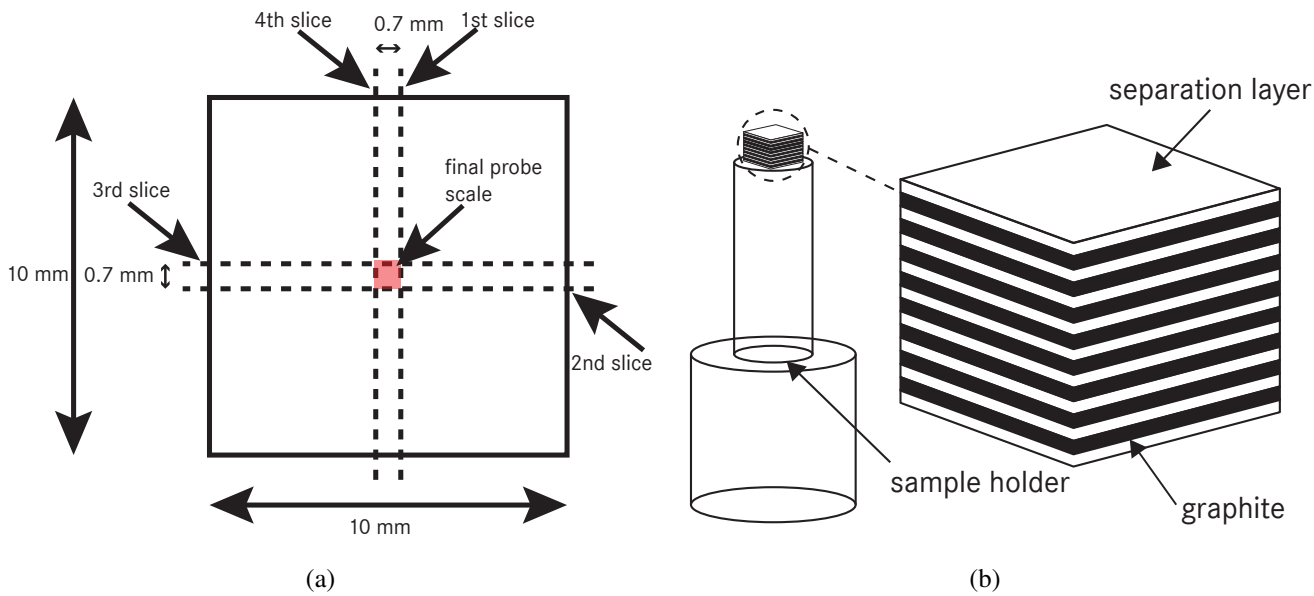

Figure 6. Through plane SEM images of a prepared anode stack

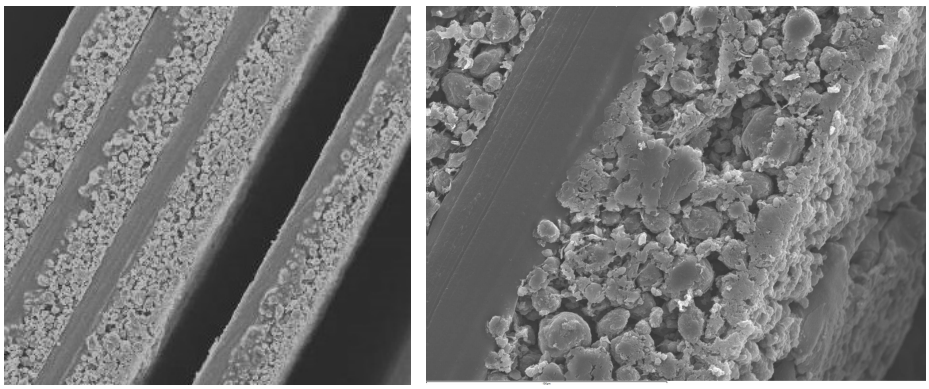

(a) Cutout with four layers (b) Cutout of two layers and the seperator

3.4. Discussion

The experimental results showed significant differences among the investigated separation material groups, see Table 2.

Double side adhesive tape showed a thickness of 35 µm and the maximum number of anode layer was obtained. The stability was very high, but due to a missing carrier a stack made from this material could not be sliced. Single side adhesive tape exhibits opposite behaviour.

Stacks consisting of microporous polymer mebranes led to the highest number of anode layers. However an additional primer (LocTite® 770) was required, because of poor adhesive properties of polypropylene (PP) and polyethylene (PE). Despite application of primer the stability of the anode layer stack was not sufficient.

The three investigated cellulose papers showed very good stacking and slicing characteristics - only differing in thickness and therefore in the amount of maximum anode layers per stack. As the best compromise between maximum number of layers and stability we selected greaseproof paper as separation material for all further stack preparations.

4. Experimental

4.1. Synchrotron Tomography

The synchrotron X-ray tomography measurements were performed at the imaging station of the BAMline [23,24]. The facility is located at the electron storage ring BESSY II at Helmholtz Centre Berlin. A monochromatic synchrotron beam at an energy level of $19\,\mathrm{keV}$ was obtained by a W-Si multilayer monochromator with an energy resolution of about $\Delta E/E = 10^{-2}$. The X-ray energy was adapted to the thickness and absorption properties of the investigated samples. It was found that $19\,\mathrm{keV}$ is a good compromise between transmission intensity and contrast. A CWO scintillator with a thickness of $50\,\mu\mathrm{m}$ was used to convert the X-rays into visible light. A PCO camera with a 4008 x 2672 pixel CCD-chip was employed to capture the images. An optical setup ("Optique-Peter") was used to transfer the light onto the CCD chip of the camera system [25], see Figure 7.

The used pixel size was $0.44\,\mu\mathrm{m}$ and the achieved spatial resolution about $1\,\mu\mathrm{m}$. The field of view was about $1.7 \times 1.2\,\mathrm{mm}^2$.

A set of 2200 radiographic images were taken from the samples over an angular range of $180°$. Additionally 230 flat field images (i.e. without sample) were taken. After subtraction of the dark field signal the radiographic projections were divided by the flat field images in order to obtain bright field corrected (normalized) images (see Figure 8(a)). Exposure time for each radiographic projection was $3\,\mathrm{s}$. Time for a complete tomographic measurement was about three hours.

Figure 7. Setup used for synchrotron tomography

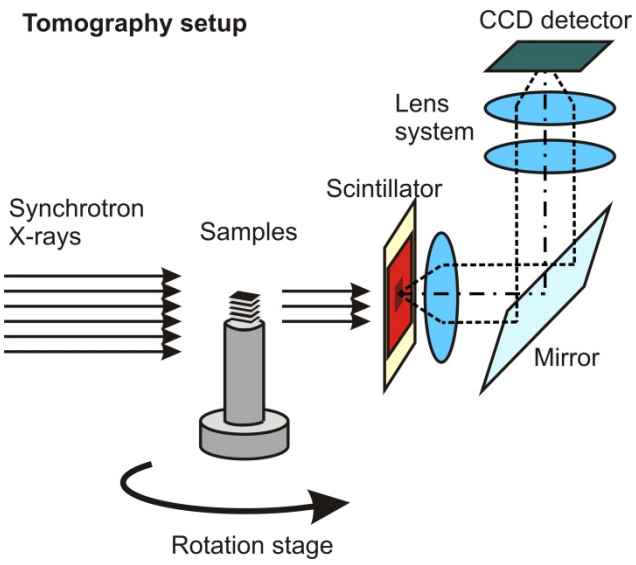

A proper normalization provides the transmission of X-rays through the sample according to the Beer-Lambert law:

$$\frac{I}{I_0} = \mathrm{e}^{\sum \mu \cdot d}$$

Here I_0 and I denote the intensity of the beam in front of and behind the sample, d the transmitted distance through a certain material and μ the linear attenuation coefficient of that material at the used X-ray energy.

4.2. Data Post-Processing

The information of the transmission was used for the three dimensional reconstruction of the attenuation coefficients of each voxel in the sample volume. This was done with a standard algorithm, the filtered-back projection [26]. Therefore the images were projected back into the volume according to the projection angle. This was applied for all angular steps. As a result the object would have been blurry. To avoid this, a high pass filter was applied to each projection in the horizontal frequency domain (Hamming filter) before back-projection. A vertical slice through the reconstructed volume is shown in Figure 8(b).

Figure 8. 2D images of a sample stack

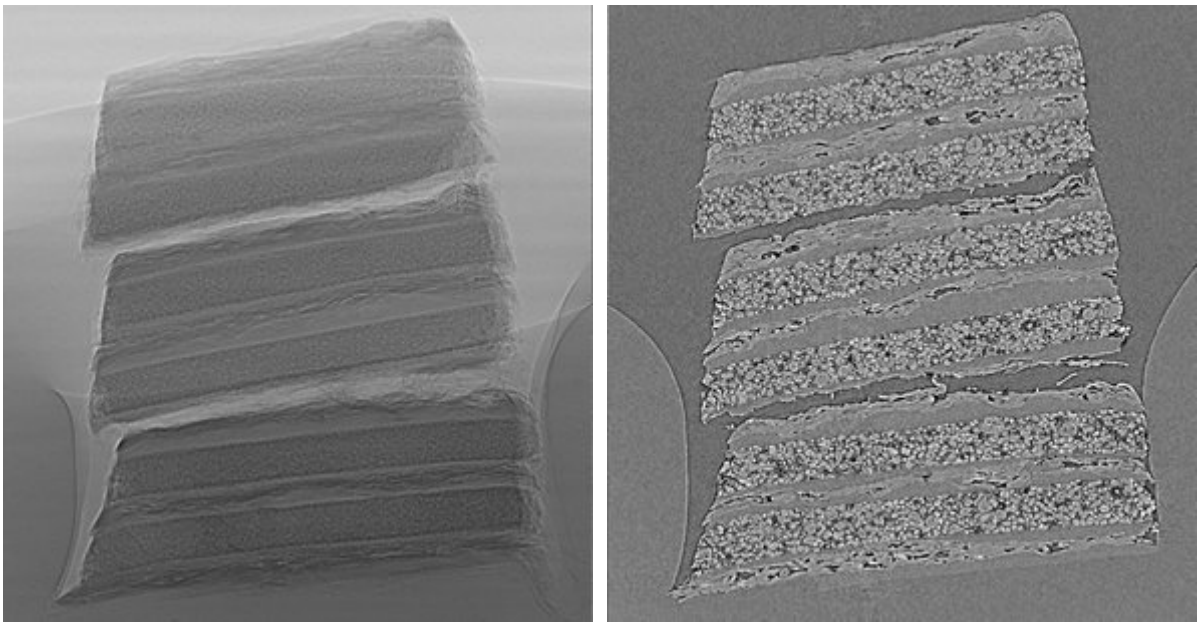

(a) Radiographic projection image (b) Reconstructed image

Since the contrast in the 3D synchrotron images is very high, we binarized those by global thresholding [27,28]. The 8-bit grayscale threshold is chosen to 32 for pristine and 72 for the degraded electrodes in order to obtain reasonable porosities between $[0.22, 0.26]$ for the samples. Figure 10 shows the effect of binarization.

5. Structural Analysis

In this section we compute several structural characteristics for images of Li-ion cells obtained by the preparation and visualization methods discussed in Sections 2 - 4. This enables us to perform a quantitative comparison and discussion of different electrode samples. Note that the considered characteristics are known to be linked to the functionality of graphite electrodes. The analysis addresses two main questions that play an important role in the investigation of Li-ion cells:

1. Can the microstructure of graphite be regarded as statistically homogeneous over the whole cell?
2. Can the influence of ageing on microstructure of graphite be characterized?

To answer these questions we take three scenarios into account where two synchrotron images for each scenario are considered. In particular, the scenarios are

(i) pristine material from the center of the cell,

(ii) pristine material from the edge of the cell,

(iii) degraded material from the center of the cell.

In the following, we denote the binary images considered for the scenarios (i)-(iii) by $\mathrm{P}^1_\mathrm{C}, \mathrm{P}^2_\mathrm{C}, \mathrm{P}^1_\mathrm{E}, \mathrm{P}^2_\mathrm{E}, \mathrm{D}^1_\mathrm{C}$ and D^2_C where P (D) stands for pristine (degraded) electrodes and C (E) for cutouts at center (edge) regions, cf. Section 2 and Figure 1(a). Recall that these images are gained as described in Sections 2 - 4. For a sample of each of the three groups see Figure 10. Note that the considered cutouts have approximately the same dimension of $660 \times 550 \times 50\ \mu\mathrm{m}^3$.

The samples analyzed in this section are extracted out of a big sized automotive EV pouch cell ($50\,\mathrm{Ah}$) nominal capacity, NMC-cathode, potential range $3\,\mathrm{V} - 4.2\,\mathrm{V}$). Degraded cell was heavily cycled for about nine months with a time-scaled realistic load profile (see Figure 9) similar to usage in a purely electric vehicle at ambient temperature of $25\,^\circ\mathrm{C}$. The final cell capacity was 70% of the initial capacity, measured with a $1\,\mathrm{C}$-discharge-current ($1\,\mathrm{C} = \frac{\mathrm{Capacity_{nom}}}{1\,\mathrm{h}}$).

Figure 9. Current profile applied to cyclically degraded cell

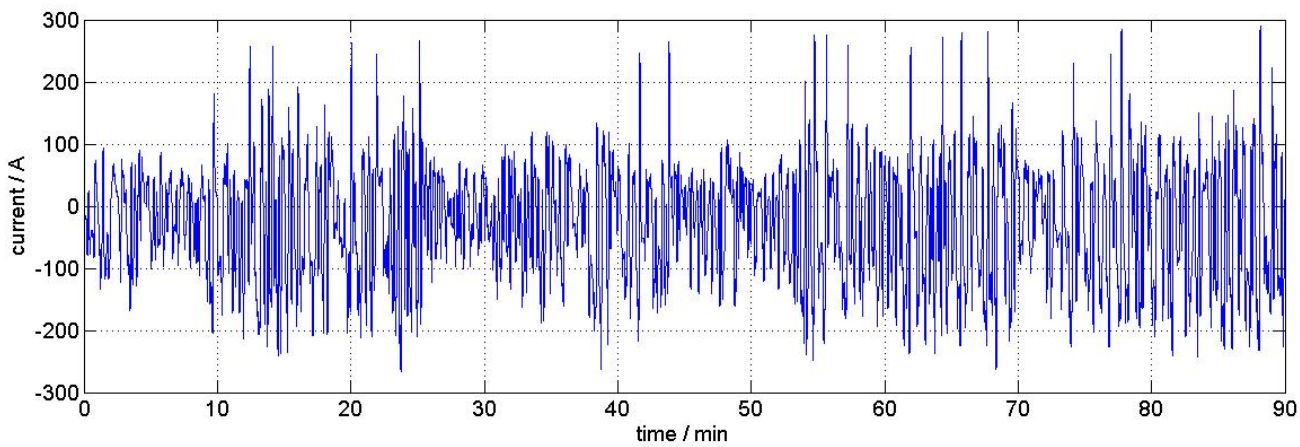

Figure 10. 2D slices from the reconstructed gray-scale (first row) and the binary (second row) images of P^1_C (left), P^2_E (center) and D^1_C (right)

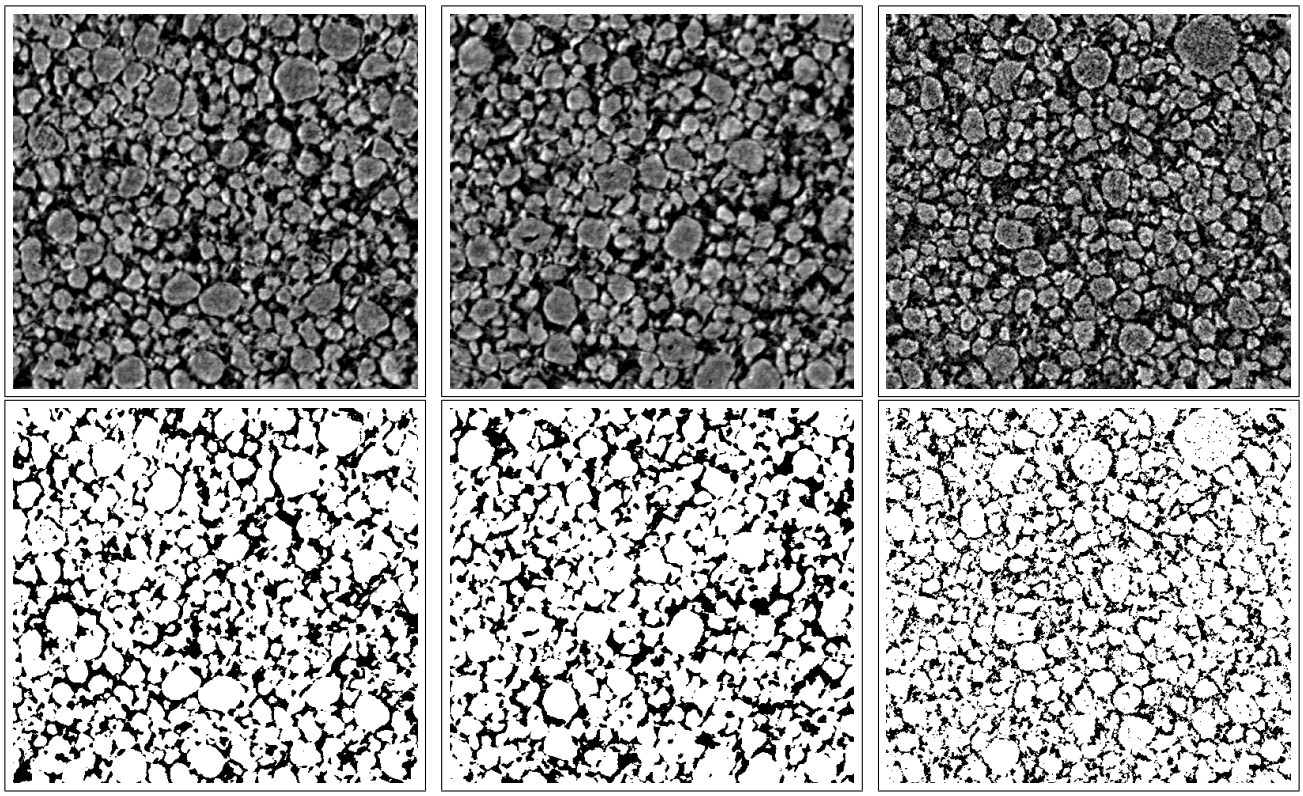

The detailed structural analysis explained below was possible due to the preparation and visualization techniques proposed in this paper.

5.1. Comparison of Structural Characteristics

The goal of this section is to obtain a quantitative comparison of the binary images $\mathrm{P}^1_\mathrm{C}, \mathrm{P}^2_\mathrm{C}, \mathrm{P}^1_\mathrm{E}, \mathrm{P}^2_\mathrm{E}, \mathrm{D}^1_\mathrm{C}$ and D^2_C by computing several structural characteristics for each of these images.

As a first structural characteristic we consider the porosity, which is the fraction of the volume of voids (i.e., volume of pore space) over the total volume [29]. The second characteristic is the specific surface area which specifies the total surface area of a material per unit volume [29].

Table 3. Porosity and specific surface area computed for six selected binary images of anode layers

	P^1_C	P^2_C	P^1_E	P^2_E	D^1_C	D^2_C
porosity	0.267	0.268	0.257	0.272	0.244	0.259
specific surface area ($^1/\mu m$)	0.435	0.44	0.416	0.434	0.594	0.588

The results obtained for the porosity and the specific surface area are listed in Table 3. It turns out that the porosities of all considered samples are nearly identical. The same holds for the specific surface areas of the pristine electrodes ($\mathrm{P}^1_\mathrm{C}, \mathrm{P}^2_\mathrm{C}, \mathrm{P}^1_\mathrm{E}, \mathrm{P}^2_\mathrm{E}$) whereas, contrarily, the specific surface areas of degraded electrodes are significantly higher than their counterparts of pristine electrodes. The microstructural characteristics of both degraded samples ($\mathrm{D}^1_\mathrm{C}, \mathrm{D}^2_\mathrm{C}$) exhibit an almost perfect match.

For a more detailed characterization of the graphite and pore space, respectively, we consider the probability density function of so-called spherical contact distances from the pore to the graphite phase and vice versa [29]. This characteristic can be interpreted as some kind of pore (particle) size distribution. The spherical contact distance of a point located in the pore phase or the graphite phase, respectively, is given by the minimum distance to the complementary phase. Note that the considered density functions uniquely determine the probability that the spherical contact distance of a randomly chosen point located in the pore phase or the graphite phase, respectively, is within a certain interval. In summary, the spherical contact distance distribution provides a good measure for the 'typical' distances from pore to graphite phase and vice versa, cf. [29].

The computed probability density functions for the spherical contact distances from graphite to pore phase and vice versa are visualized in Figures 12(a) and 12(b), respectively. The corresponding mean values and variances are listed in Table 4. It turns out that the density functions for the spherical contact distances computed for $(\mathrm{P}_{\mathrm{C}}^1, \mathrm{P}_{\mathrm{C}}^2, \mathrm{P}_{\mathrm{E}}^1, \mathrm{P}_{\mathrm{E}}^2)$ nearly coincide whereas a large discrepancy is observed between the results for pristine and degraded electrodes. In particular, for both the spherical contact distances from graphite to pore phase and vice versa, these distances are by trend smaller for the degraded electrodes compared to the pristine electrodes. This coherence can be explained by cracks and fractures in the microstructures of degraded electrodes. These deformations lead to a much finer dispersed graphite phase within the degraded electrodes whereas the graphite phase in the pristine electrodes is much more aggregated. This assumption is also supported by the visual impression of Figure 10.

Finally we focus on the so-called geometric tortuosity, see e.g. [30–32]. It evaluates the tortuosity of the pathways through the pore phase in through-plane direction. In particular, starting from a randomly chosen location on top of the porous material, the geometric tortuosity is defined as the random Euclidean length of its shortest path through the material along all possible paths within the pore space divided by the material thickness (in z-direction). For this purpose, the set of pore space paths is represented by a geometric 3D graph. This graph is computed using the skeletonization algorithm implemented in the software Avizo 7, see Figure 11.

Figure 11. Extraction of pore space graph via skeletonization from a 3D binary image: binary image (left); solid phase and pore space graph (center); pore space graph (right)

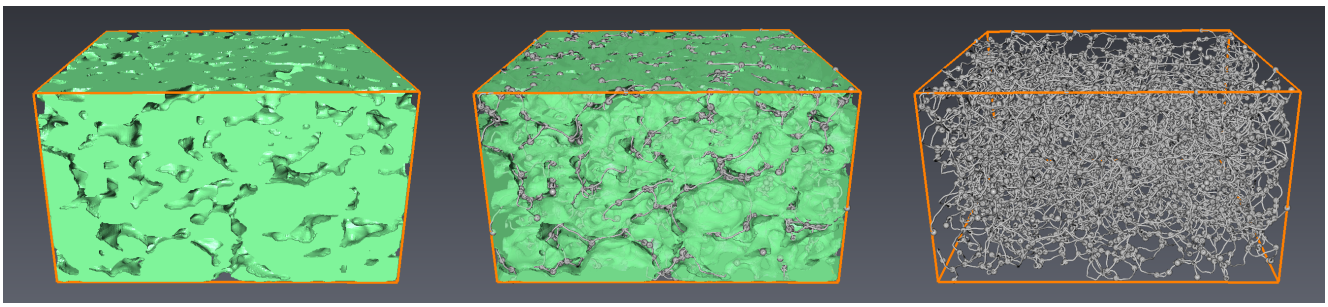

The computed probability density functions for the geometric tortuosity are visualized in Figure 12(c) whereas the corresponding mean values and variances are listed in Table 4. As result we again obtain that the differences of geometric tortuosity within both groups (i.e., pristine $\mathrm{P}_{\mathrm{C}}^1, \mathrm{P}_{\mathrm{C}}^2, \mathrm{P}_{\mathrm{E}}^1, \mathrm{P}_{\mathrm{E}}^2$ and degraded $\mathrm{D}_{\mathrm{C}}^1$, $\mathrm{D}_{\mathrm{C}}^2$ electrodes) are negligible. Moreover, there exist significant deviations between the two groups where the degraded electrodes have significantly smaller values of the length of shortest pathways through their

pore space. This can be again explained by the much finer dispersed graphite phase within degraded electrodes.

Figure 12. Probability density functions for structural characteristics of graphite layers

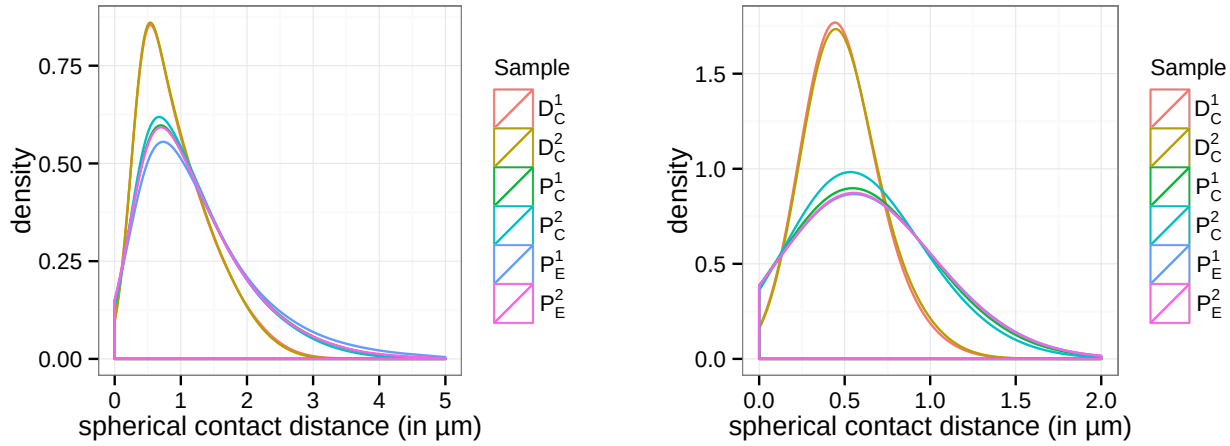

(a) Spherical contact distances from graphite to pore phase (b) Spherical contact distances from pore to graphite phase

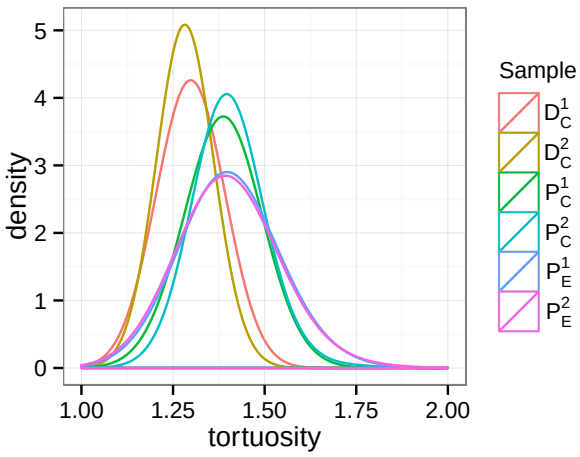

(c) Geometric tortuosity

5.2. Summary

In this section we summarize the discussion of the results obtained by the structural analysis. It turns out that for all considered characteristics the differences within the pristine and degraded groups are negligible whereas a significant discrepancy between the two groups can be observed. In particular, we can conclude that it does not matter from which region of the tomograms the cutouts are extracted. This also indicates that the considered materials are perfectly homogeneous. Moreover, because of the structural differences between pristine and degraded electrodes we can conclude that synchrotron tomography is an adequate method to detect such changes. Thus, the proposed preparation and visualization techniques described in Sections 3 and 4 provides an excellent tool for a cost- and time-saving analysis of degradation processes in the microstructure of Li-ion cells.

Table 4. Mean and variance of the spherical contact distances for pore ($\mathrm{scdf_P}$) and graphite phase ($\mathrm{scdf_{graphite}}$) in µm as well as of the geometric tortuosity (tort) computed for six selected binary images of anode layers

	$\mathrm{P_C^1}$	$\mathrm{P_C^2}$	$\mathrm{P_E^1}$	$\mathrm{P_E^2}$	$\mathrm{D_C^1}$	$\mathrm{D_C^2}$
$\mathrm{scdf_P}$ mean	1.176	1.152	1.275	1.184	0.92	0.915
$\mathrm{scdf_P}$ variance	0.578	0.523	0.795	0.608	0.279	0.267
$\mathrm{scdf_{graphite}}$ mean	0.596	0.59	0.606	0.604	0.483	0.493
$\mathrm{scdf_{graphite}}$ variance	0.06	0.058	0.064	0.063	0.02	0.023
tort mean	1.386	1.403	1.405	1.401	1.298	1.284
tort variance	0.004	0.005	0.007	0.008	0.003	0.002

6. Conclusion

We successfully introduced a new preparation method for analysis of Li-ion graphite material using synchrotron tomography. The complete procedure including cell disassembly, sample selection and extraction as well as proposed efficient multilayer stacking were described in detail.

Due to discussed complex ageing behaviour of Li-ion cells many investigations have to be done to gain a more detailed understanding. Particularly anode material is a key factor for cell-performance and limitation of lifetime. Since the microstructure of active material is essential for ageing characteristics, synchrotron tomography is an excellent method, because the resolution is high enough to detect the shape of particles and the differences between particles and pores in all three dimensions.

The presented preparation method extends the advantages of synchrotron tomography by massively parallel measurement of samples. This results in the possibility to compare different regions of a given cell, enhance statistical data due to analyzing many samples from a similar area of a cell, compare anode material from different manufactures or cells and in lower costs, because less measurements are necessary.

As shown in Section 5 structural analysis pointed out that ageing causes significant changes in microstructure of graphite material. Furthermore we found out that investigated samples from the same cell do not significantly differ from a statistical point of view. Hence the method provides the possibility to analyze homogeneity of used active material. On the other hand the difference between pristine and aged cells, with respect to calculated characteristics, e.g. tortuosity and sizes of pores and particles, is significant which leads us to more detailed analyses and investigations like (functional) particle-based modelling to be done as future work. Furthermore structural characteristics of lithium deposition, which can be made visible in synchrotron tomography using the method proposed in Section 2.4 will be investigated in a forthcomming paper.

Acknowledgements

Gerd Gaiselmann and Volker Schmidt gratefully acknowledge funding of the present research by the German Federal Ministry for Education and Science (BMBF) in the framework of the priority program 'Mathematics for Innovations in Industry and Services' under grant number 05M13VUA.

References

1. Vetter, J.; Novák, P.; Wagner, M.; Veit, C.; Möller, K.C.; Besenhard, J.; Winter, M.; Wohlfahrt-Mehrens, M.; Vogler, C.; Hammouche, A. Ageing mechanisms in lithium-ion batteries. *Journal of Power Sources* **2005**, *147*, 269 – 281.
2. Agubra, V.; Fergus, J. Lithium ion battery anode aging mechanisms. *Materials* **2013**, *6*, 1310–1325.
3. Winter, M. The solid electrolyte interphase - the most important and the least understood solid electrolyte in rechargeable Li batteries. *International Journal of Research in Physical Chemistry and Chemical Physics.* **2009**, *223*, 1395–1406.
4. Gnanaraj, J.S.; Thompson, R.W.; Iaconatti, S.N.; DiCarlo, J.F.; Abraham, K.M. Formation and growth of surface films on graphitic anode materials for Li-ion batteries. *Electrochemical and Solid-State Letters* **2005**, *8*, A128–A132.
5. Ploehn, H.J.; Ramadass, P.; White, R.E. Solvent diffusion model for aging of lithium-ion battery cells. *Journal of The Electrochemical Society* **2004**, *151*, A456–A462.
6. Arora, P.; Doyle, M.; White, R.E. Mathematical modeling of the lithium deposition overcharge reaction in lithium-ion batteries using carbon-based negative electrodes. *Journal of The Electrochemical Society* **1999**, *146*, 3543–3553.
7. Fan, J.; Tan, S. Studies on charging lithium-ion cells at low temperatures. *Journal of The Electrochemical Society* **2006**, *153*, A1081–A1092.
8. Tippmann, S.; Walper, D.; Balboa, L.; Spier, B.; Bessler, W.G. Low-temperature charging of lithium-ion cells part I: Electrochemical modeling and experimental investigation of degradation behavior. *Journal of Power Sources* **2014**, *252*, 305–316.
9. Barai, P.; Simunovic, S.; Mukherjee, P.P. Damage and crack analysis in a Li-ion battery electrode using random spring model. *ASME 2012 International Mechanical Engineering Congress and Exposition* **2012**, *6*, 483–486.
10. Shearing, P.; Howard, L.; Jørgensen, P.; Brandon, N.; Harris, S. Characterization of the 3-dimensional microstructure of a graphite negative electrode from a Li-ion battery. *Electrochemistry Communications* **2010**, *12*, 374–377.
11. Manke, I.; Banhart, J.; Haibel, A.; Rack, A.; Zabler, S.; Kardjilov, N.; Hilger, A.; Melzer, A.; Riesemeier, H. In situ investigation of the discharge of alkaline Zn-MnO2 batteries with synchrotron X-ray and neutron tomographies. *Applied Physics Letters* **2007**, *90*, 214102.
12. Ebner, M.; Marone, F.; Stampanoni, M.; Wood, V. Visualization and quantification of electrochemical and mechanical degradation in Li ion batteries. *Science* **2013**, *342*, 716–720.

13. Ebner, M.; Geldmacher, F.; Marone, F.; Stampanoni, M.; Wood, V. Electrode materials: X-ray tomography of porous, transition metal oxide based lithium ion battery electrodes. *Advanced Energy Materials* **2013**, *3*, 825–825.
14. Zielke, L.; Hutzenlaub, T.; Wheeler, D.R.; Manke, I.; Arlt, T.; Paust, N.; Zengerle, R.; Thiele, S. A combination of X-ray tomography and carbon binder modeling: reconstructing the three phases of LiCoO2 Li-ion battery cathodes. *Advanced Energy Materials* **2014**.
15. Stenzel, O.; Westhoff, D.; Manke, I.; Kasper, M.; Kroese, D.P.; Schmidt, V. Graph-based simulated annealing: a hybrid approach to stochastic modeling of complex microstructures. *Modelling and Simulation in Materials Science and Engineering* **2013**, *21*, 055004.
16. Haibel, A.; Manke, I.; Melzer, A.; Banhart, J. In situ microtomographic monitoring of discharging processes in alkaline cells. *Journal of The Electrochemical Society* **2010**, *157*, A387–A391.
17. Hoch, C.; Schier, H.; Kallfass, C.; Tötzke, C.; Hilger, A.; Manke, I. Electrode deterioration processes in lithium ion capacitors monitored by in situ X-ray radiography on micrometre scale. *Micro Nano Letters, IET* **2012**, *7*, 262–264.
18. Schröder, D.; Arlt, T.; Krewer, U.; Manke, I. Analyzing transport paths in the air electrode of a zinc air battery using X-ray tomography. *Electrochemistry Communications* **2014**, *40*, 88 – 91.
19. Banhart, J.; Borbely, A.; Dzieciol, K.; Garcia-Moreno, F.; Manke, I.; Kardjilov, N.; Kaysser-Pyzalla, A.R.; Strobl, M.; Treimer, W. X-ray and neutron imaging - Complementary techniques for materials science and engineering. *International Journal of Materials Research* **2010**, *101*, 1069–1079.
20. Epstein, N. On tortuosity and the tortuosity factor in flow and diffusion through porous media. *Chemical Engineering Science* **1989**, *44*, 777–779.
21. Monthioux, M.; Smith, B.; Burteaux, B.; Claye, A.; Fischer, J.; Luzzi, D. Sensitivity of single-wall carbon nanotubes to chemical processing: an electron microscopy investigation. *Carbon* **2001**, *39*, 1251–1272.
22. Zhang, S.S. A review on the separators of liquid electrolyte Li-ion batteries. *Journal of Power Sources* **2007**, *164*, 351–364.
23. Görner, W.; Hentschel, M.; Müller, B.; Riesemeier, H.; Krumrey, M.; Ulm, G.; Diete, W.; Klein, U.; Frahm, R. BAMline: the first hard X-ray beamline at BESSY II. *Nuclear Instruments and Methods in Physics Research Section A: Accelerators, Spectrometers, Detectors and Associated Equipment* **2001**, *467-468, Part 1*, 703–706. 7th Int.Conf. on Synchrotron Radiation Instrumentation.
24. Manke, I.; Markötter, H.; Tötzke, C.; Kardjilov, N.; Grothausmann, R.; Dawson, M.; Hartnig, C.; Haas, S.; Thomas, D.; Hoell, A.; Genzel, C.; Banhart, J. Investigation of energy-relevant materials with synchrotron X-rays and neutrons. *Advanced Engineering Materials* **2011**, *13*, 712–729.
25. Williams, S.H.; Hilger, A.; Kardjilov, N.; Manke, I.; Strobl, M.; Douissard, P.A.; Martin, T.; Riesemeier, H.; Banhart, J. Detection system for microimaging with neutrons. *Journal of Instrumentation* **2012**, *7*, P02014.

26. Banhart, J. *Advanced Tomographic Methods in Materials Research and Engineering*; Oxford University Press, 2008.
27. Burger, W.; Burge, M.J. *Digital Image Processing: An Algorithmic Introduction Using Java*; Springer, 2008.
28. Jähne, B. *Digital Image Processing*; Springer, 2005.
29. Chiu, S.N.; Stoyan, D.; Kendall, W.S.; Mecke, J. *Stochastic Geometry and its Applications*; Wiley, 2013.
30. Gaiselmann, G.; Neumann, M.; Schmidt, V.; Pecho, O.; Hocker, T.; Holzer, L. Quantitative relationships between microstructure and effective transport properties based on virtual materials testing. *American Institute of Chemical Engineers Journal* **2014**, *60*, 1983–1999.
31. Tötzke, C.; Gaiselmann, G.; Osenberg, M.; Bohner, J.; Arlt, T.; Markötter, H.; Hilger, A.; Wieder, F.; Kupsch, A.; Müller, B.; Hentschel, M.; Banhart, J.; Schmidt, V.; Lehnert, W.; Manke, I. Three-dimensional study of compressed gas diffusion layers using synchrotron X-ray imaging. *Journal of Power Sources* **2014**, *253*, 123–131.
32. Gaiselmann, G.; Tötzke, C.; Manke, I.; Lehnert, W.; Schmidt, V. 3D microstructure modeling of compressed fiber-based materials. *Journal of Power Sources* **2014**, *257*, 52–64.